

Understanding Normalization in Contrastive Representation Learning and Out-of-Distribution Detection

Tai Le-Gia, Jaehyun Ahn

Abstract—Contrastive representation learning has emerged as an outstanding approach for anomaly detection (AD). In this work, we explore the ℓ_2 -norm of contrastive features and its applications in out-of-distribution detection. We propose a simple method based on contrastive learning, which incorporates out-of-distribution data by discriminating against normal samples in the contrastive layer space. Our approach can be applied flexibly as an outlier exposure (OE) approach, where the out-of-distribution data is a huge collective of random images, or as a fully self-supervised learning approach, where the out-of-distribution data is self-generated by applying distribution-shifting transformations. The ability to incorporate additional out-of-distribution samples enables a feasible solution for datasets where AD methods based on contrastive learning generally underperform, such as aerial images or microscopy images. Furthermore, the high-quality features learned through contrastive learning consistently enhance performance in OE scenarios, even when the available out-of-distribution dataset is not suitable. Our extensive experiments demonstrate the superiority and robustness of our proposed method under various scenarios, including unimodal and multimodal settings, with various image datasets. The reproducible code is available at https://github.com/nguoikhongnao/real_OECL.

Index Terms—Anomaly Detection, Outlier Exposure, Contrastive Learning, Unsupervised Learning.

I. INTRODUCTION

Out-of-distribution (OOD) detection, or anomaly detection (AD), is the task of distinguishing between normal and out-of-distribution (abnormal) data, with the general assumption that access to abnormal data is prohibited. Therefore, OOD detection methods [14, 18, 43] are typically carried out in an unsupervised manner where only normal data is available. In this regard, approaches based on self-supervised learning or pre-trained models, which are capable of extracting deep features without explicitly requiring labeled data, are commonly utilized to solve OOD detection problems.

However, the presumption that access to non-nominal data is forbidden is not highly restricted. Especially in image OOD detection problems, one can gather randomly image datasets that are likely not-normal on the internet. The utilization of such data is called Outlier Exposure [17]. Several top-performing AD methods, including unsupervised [29], self-supervised [18], and pre-trained [35, 10] approaches, utilize tens of thousands of OE samples to enhance their performance and achieve state-of-the-art detection accuracy. Nevertheless, it is important to note

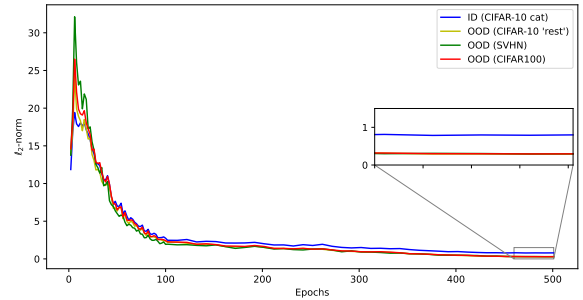


Fig. 1: The ℓ_2 -norm of contrastive features for both normal and OOD samples during optimization of $\mathcal{L}_{\text{contrastive}}$ using only normal samples. Following a few epochs of rapid increase, the ℓ_2 -norm for both normal and OOD samples gradually decreases. Notably, as training progresses, the ℓ_2 -norm of the training samples becomes larger than that of the OOD samples.

that Outlier Exposure (OE) also has its limitations, especially when the normal data is highly diverse [29], or when the OE datasets are not suitable, as demonstrated in our experiments.

One of the most effective OOD detection techniques, CSI [43] is constructed by combining a special form of contrastive learning, SimCLR [7], with a geometric OOD detection approach [18]. SimCLR encourages augmented views of a sample to attract each other while repelling them to a negative corpus consisting of views of other samples. CSI suggests that the addition of sufficiently distorted augmentations to the negative corpus improves OOD detection performance. Simultaneously, the network has to classify each sample's type of transformation, as in [18]. For a test sample, the anomaly score is determined by both the trained network's confidence in correctly predicting the sample's transformations and the sample's similarity to its nearest neighbor in the feature space. However, similar to geometric approaches [14, 18], CSI performance depends on the relationship between normal data and shifted transformations (e.g., symmetry images and rotations).

Inspired by the strengths and weaknesses of both approaches, we propose *Outlier Exposure framework for Contrastive Learning* (OECL), an OE extension for contrastive learning OOD detection methods. By manipulating the ℓ_2 -norm of samples on the contrastive space, we found a simple way to integrate OOD samples into SimCLR-based methods. The

Tai Le-Gia and Jaehyun Ahn are with the Department of Mathematics, Chungnam National University, Daejeon, South Korea (Email: vip-giatailhp@gmail.com; jhahn@cnu.ac.kr).

high quality deep representations obtained by contrastive learning and the “anomalousness” from OOD samples allow our proposed method to address the limitations of the both original approaches. To validate our claims, we conducted extensive experiments in various environments, including the common unimodal setting, the newly challenging multimodal setting. Our main contributions are summarized as follows:

- 1) We propose a simple yet effective and robust method, OECL, to incorporate out-of-distribution data to contrastive learning OOD methods. The out-of-distribution data can be selected from an external out-of-distribution dataset or self-generated by sufficiently distorted transformations.
- 2) We provide insight into the ℓ_2 -normalization in contrastive learning and its application in OOD detection.
- 3) We empirically study the *diminishing effect* of OE-based models, where “far” OE datasets might have negative impacts to AD performance.

The remaining sections of the paper are organized as follows. Section II introduces previous works related to ours. Section III presents SimCLR and theoretical results regarding the ℓ_2 -norm of contrastive features, as well as our proposed OECL. Extensive experiments and analysis are provided in Section IV, where we also study the diminishing effect. Section V discusses the applicability of OECL and other OE-based methods. We conclude the paper in Section VI.

II. RELATED WORK

OOD detection. A growing area of research uses self-supervision [7, 20, 13] for OOD detection. They train a network with a pre-defined task on the training set and utilize the rich features to improve OOD detection performances. These approaches have demonstrated remarkable performance in OOD detection, pushing the boundaries of what is achievable in this field [14, 18, 47, 43, 42].

More recently, transfer learning-based methods have revolutionized OOD detection [4, 10, 35, 29, 9, 32, 26]. These approaches involve fine-tuning supervised classifiers that were originally trained on large datasets [29, 34]. This fine-tuning process adapts these classifiers to OOD detection tasks and has been shown to outperform the self-supervised methods on common benchmarks. However, the generalization of transfer learning-based methods to specialize data remain a concern.

Another research field in OOD detection is about incorporating outliers to improve the performance of unsupervised OOD detection methods [17, 38, 23, 29, 40, 28]. For instance, [17] uses OE to improve their self-supervised method by forcing the network to predict the uniform distribution for OE samples. [3] uses OE as a penalty to hinder the student model from generalizing its imitation of the teacher model to out-of-distribution images.

Non-standard image OOD detection. Recently, there has been a growing interest in “non-standard” image OOD detection. Unlike the common CIFAR-10 or ImageNet, these non-standard datasets have unique characteristics that challenge OOD detection methods. One such challenge is presented by datasets where normal and abnormal samples are semantically

identical but differ in their local appearances. Datasets with such a characteristic are primarily objects in defect detection research [36, 3, 28]. Another category of non-standard datasets arises from the distinctive physical properties of training images, such as rotation-invariant images. In these cases, recent unsupervised methods [14, 43] have faced limitations as shown in our experiments. Datasets belong to this ‘distinctive physical’ category and standard images are our main focus in this paper.

Embedding norm of normalized soft-max. It has been observed that a normalized softmax model trained on normal data tends to yield larger feature norms over normal samples compared to OOD instances, especially in face recognition learning [6, 31, 50]. NAE [6] uses ℓ_2 -norm of features as the binary person/background classification confidence. MagFace [31] assumes a positive correlation between the norm and quality of features, and use the embedding norm to penalize low-quality face samples and reward high-quality ones. In the context of general anomaly detection, CSI [43] suggests using product of ℓ_2 -norm of contrastive features along with cosine similarity as the anomaly detection score.

III. CONTRASTIVE LEARNING AND ANOMALY DETECTION

Suppose we are given an unlabeled dataset $\mathcal{D} = \{x_i\}_{i=1}^N$ sampled from a distribution $p_{\text{data}}(x)$ over \mathbb{R}^n . The goal of anomaly detection is to construct a detector that identifies whether x is sampled from p_{data} or not. However, directly modeling an accurate model of p_{data} is impractical or infeasible in most cases. To address this, many existing approaches to anomaly detection instead rely on defining a scoring function $s(x)$, with a high value indicating that x is likely to belong to the in-distribution.

A. Normalization in Contrastive Learning

Contrastive learning framework. Contrastive learning aims to learn an encoder by maximizing agreement between positive pairs. Empirically, given a set of pre-determined transformations T , positive pairs are obtained by applying randomly two transformations to the same sample, e.g., two affine transformations of the same picture x [2, 7, 16]. These positive samples are also regarded as a surrogate class of x [12]. In this paper, we investigate the specific and widely popular form of contrastive loss where the training encoder $z(x) \triangleq f(x)/\|f(x)\| : \mathbb{R}^n \rightarrow S^{m-1}$ maps data to a hypersphere of dimension $m-1$. This loss has been outstandingly successful in anomaly detection literature [43, 41, 52],

$$\mathcal{L}_{\text{contrastive}}(z; \tau, M) \triangleq \mathbb{E}_{\substack{(x,y) \sim p_{\text{pos}} \\ \{x_i^-\}_{i=1}^M \stackrel{\text{i.i.d.}}{\sim} p_{\text{data}}}} \left[-\log \frac{e^{z(x)^t z(y)/\tau}}{e^{z(x)^t z(y)} + \sum_i e^{z(x_i^-)^t z(y)/\tau}} \right], \quad (2)$$

where τ is a temperature hyperparameter, M is a fixed number of negative samples in a mini-batch and p_{pos} is the distribution of positive pairs over $\mathbb{R}^n \times \mathbb{R}^n$. This loss can be decoupled into *alignment loss* and *uniformity loss* as in [48]:

$$\mathcal{L}_{\text{align}} = \mathbb{E}_{(x,y) \sim p_{\text{pos}}} [-z(x)^t z(y)/\tau] \quad (3)$$

$$\mathcal{L}_{\text{uniform}} = \mathbb{E}_{\substack{(x,y) \sim p_{\text{pos}} \\ \{x_i^-\}_{i=1}^M \stackrel{\text{i.i.d.}}{\sim} p_{\text{data}}}} \left[\log \left(e^{z(x)^t z(y)} + \sum_i e^{z(x_i^-)^t z(y)/\tau} \right) \right] \quad (4)$$

The first term $\mathcal{L}_{\text{align}}$ encourages samples from the same surrogate class be mapped to nearby features. Meanwhile, $\mathcal{L}_{\text{uniform}}$ maximizes averages distances between all samples, leading to features vectors roughly uniformly distributed on the unit hypersphere \mathcal{S}^{m-1} [48].

B. The ℓ_2 -norm of contrastive features

In the field of anomaly detection, it is observed that a normalized soft-max model trained on the normal data exhibits larger values of feature norm over normal samples than the OOD instances [6, 50, 31, 46]. Particularly, CSI [43] suspects that ‘‘increasing the norm maybe an easier way to maximize cosine similarity between two vectors: instead of directly reducing the feature distance of two augmented samples, one can also increase the overall norm of the features to reduce the relative distance of two samples’’. Our study sheds further light on the behavior of the ℓ_2 -norm: contrastive learning gradually reduces the ℓ_2 -norm of contrastive features, while the alignment loss compels a significantly larger ℓ_2 -norm for the contrastive features of training samples.

Gradual reduction of the ℓ_2 -norm of contrastive features.

This is a phenomenon we observed in many settings using contrastive loss functions based on cosine similarity. As illustrated in Figure 1, following a few epochs of rapid increase, the ℓ_2 -norm of both normal and OOD samples gradually decreases. We suspect that this phenomenon is a natural outcome of employing cosine similarity along the interaction between $\mathcal{L}_{\text{align}}$ and $\mathcal{L}_{\text{uniform}}$. We provide further detailed analysis and experiments about this phenomenon in Appendix B.

A larger ℓ_2 -norm of normal contrastive features. As training progresses, the ℓ_2 -norm of the normal samples becomes larger than that of the OOD samples. To understand this behavior, let’s assume that the surrogate classes $\{f(t(x))\}_{t \sim T}$ are normally distributed. Since the cosine between two vectors is invariant under rotations, we can assume without loss of generality that $\mathbb{E}_{t \sim T} f(t(x)) = (\mu, 0, \dots, 0)$. The following theorem provides a clear illustration of the relationship between contrastive features and alignment in contrastive learning.

Theorem III.1. *Given two vectors $\mathbf{X} = (X_1, X_2, \dots, X_n)^t$ and $\mathbf{Y} = (Y_1, Y_2, \dots, Y_n)^t$ are i.i.d $\mathcal{N}(\boldsymbol{\mu}, \boldsymbol{\Sigma})$ where $\boldsymbol{\mu} = (\mu, 0, \dots, 0)^t$, $\mu \geq 0$ and $\boldsymbol{\Sigma} = \begin{bmatrix} \sigma & \mathbf{0} \\ \mathbf{0} & \Sigma_V \end{bmatrix}$. Then,*

1) $\mathbb{E} \left\langle \frac{\mathbf{X}}{\|\mathbf{X}\|}, \frac{\mathbf{Y}}{\|\mathbf{Y}\|} \right\rangle$ is an increasing function of μ

2) The following inequalities hold for all $\epsilon > 0$

$$\mathbb{E} \left\langle \frac{\mathbf{X}}{\|\mathbf{X}\|}, \frac{\mathbf{Y}}{\|\mathbf{Y}\|} \right\rangle \leq \left(\Phi \left(\frac{\mu}{\sigma} \right) - \Phi \left(-\frac{\mu}{\sigma} \right) \right)^2, \quad (5)$$

$$\mathbb{E} \left\langle \frac{\mathbf{X}}{\|\mathbf{X}\|}, \frac{\mathbf{Y}}{\|\mathbf{Y}\|} \right\rangle \geq \frac{1}{1 + \frac{\sigma_V^2}{\epsilon^2 \mu^2}} \left(\Phi \left(\frac{(1-\epsilon)\mu}{\sigma} \right) - \Phi \left(-\frac{(1+\epsilon)\mu}{\sigma} \right) \right)^2, \quad (6)$$

where $\sigma_V^2 = \text{tr}(\Sigma_V)$ and Φ is the cumulative distribution function of $\mathcal{N}(0, 1)$.

See proof on page 11.

Theorem III.1 emphasizes the significance of both ratios μ/σ and μ/σ_V in the minimization of $\mathcal{L}_{\text{align}}$. The inequality (5) demonstrates that without a sufficiently large ratio μ/σ , the cosine similarity between positive pairs cannot be maximized effectively, even when the variance of the contrastive feature projection onto the hyperspace perpendicular to $\mathbb{E}(f_t(x))$ is small ($\Sigma_V \sim 0$). Moreover, as $\mu \rightarrow \infty$ for fixed σ and σ_V , the right-hand side of (6) converges to 1. This means that optimizing μ is an effective way to maximize the cosine similarity of the augmentations, as illustrated in Figure 8. The above observations indicate that, in the context of contrastive learning, the encoder undergoes a learning process that encourages a sufficiently large norm of the contrastive feature of training samples, thereby facilitating alignment.

C. The ℓ_2 -norm of contrastive features: more than an anomaly score

As discussed in Section III-A, the normalization in contrastive learning inherently promotes a large norm for the contrastive features over training samples rather than samples from an out-of-distribution dataset; it naturally creates a separation between in-distribution data and out-of-distribution data on the contrastive feature space. Exploiting this characteristic, CSI uses the ℓ_2 -norm of contrastive features as a powerful tool for detecting anomalies, which has been experimentally shown to be remarkably effective [43]. Beyond a tool used in inference time, we propose to utilize the ℓ_2 -norm as a component in the encoder training process.

Outlier exposure for contrastive learning. Our key finding is that we can further increase this separation by simply forcing the encoder to produce *zero*-values contrastive features for many augmentations of out-of-distribution samples, thus improving the anomaly detection capabilities. In this paper, we consider a specific out-of-distribution dataset, referred to as *outlier exposure* dataset, denoted as \mathcal{D}_{oe} . We define the general form of our proposed *outlier exposure contrastive learning* loss as follows:

$$\mathcal{L}_{\text{oecl}} \triangleq \mathcal{L}_{\text{contrastive}}(z; \tau, M) + \alpha \mathbb{E}_{x \in \mathcal{D}_{\text{oe}}, t \in T_{\text{oe}}} \|f(t(x))\|_2, \quad (7)$$

where α is a balancing hyper-parameter, and T_{oe} is a set of transformations for OE augmentations. Typically, T_{oe} is set equal to the set of augmentations T . \mathcal{D}_{oe} can either consist of randomly collected images in terms of outlier exposure [17, 29], or be generated through distributional-shifting transformations

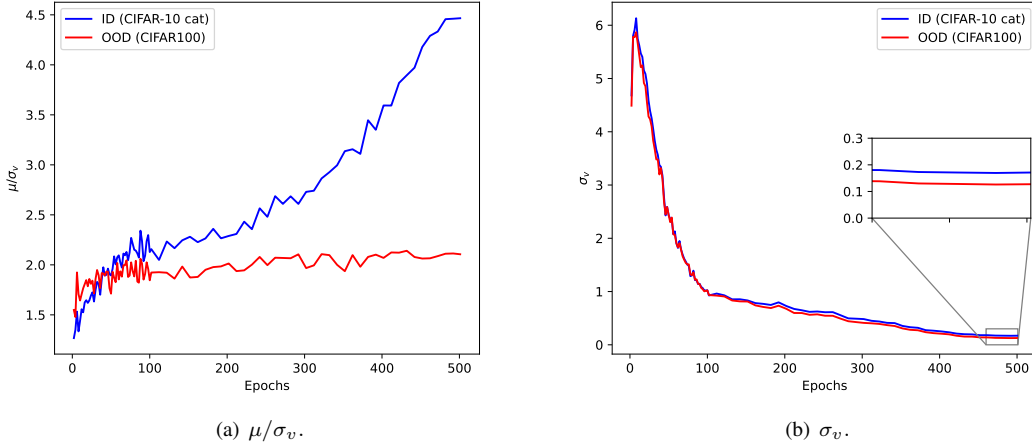


Fig. 2: Averages of μ/σ_v and σ_v for both normal and OOD samples during the optimization of $\mathcal{L}_{\text{contrastive}}$ using only normal samples. While there is only a minimal difference in σ_v between normal and OOD samples, the ratio μ/σ_v for normal samples becomes significantly larger as the training progresses.

as employed in CSI [43]. This versatility allows our proposed approach to be interpreted as an outlier exposure extension for contrastive learning or a fully self-supervised generalization of CSI and SimCLR. Specifically, in the later setting, we consider a family of augmentations \mathcal{S}_{oe} , which we call *outlier exposure transformations*. These transformations satisfy that for any $S \in \mathcal{S}_{\text{oe}}$, $S(x)$ can be regarded as an outlier with respect to any data joining $\mathcal{L}_{\text{contrastive}}$. It is worth noting that if $\mathcal{L}_{\text{contrastive}}$ is CSI, then \mathcal{S}_{oe} does not contain any elements from the distribution-shifting transformations \mathcal{S} of CSI, i.e., $\mathcal{S}_{\text{oe}} \cap \mathcal{S} = \emptyset$. The *self-outlier-exposure contrastive learning* loss is given by,

$$\mathcal{L}_{\text{oecl}} = \mathcal{L}_{\text{contrastive}}(z; \tau, M) + \alpha \mathbb{E}_{x \in \mathcal{S}_{\text{oe}}(\mathcal{D}), t \in T_{\text{oe}}} \|f(t(x))\|_2, \quad (8)$$

where $\mathcal{S}_{\text{oe}}(\mathcal{D}) \triangleq \{S(x)\}_{S \in \mathcal{S}_{\text{oe}}, x \in \mathcal{D}}$.

Score functions for detecting anomalies. Upon the contrastive feature $f(\cdot)$ learned by our proposed training objective, we define several score functions for deciding whether a given sample x is normal or not. All of our score functions follow the conventional philosophy that in-distribution samples have higher scores. The most obvious choices are ℓ_2 -norm of the contrastive feature and its ensemble version over random augmentations.

$$\text{Non-ensemble : } \quad s_{\ell_2} \triangleq \|f(x)\|_2^2, \quad (9)$$

$$\text{Ensemble : } \quad s_{\mu} \triangleq \|\mathbb{E}_{t \in T} f(t(x))\|_2^2. \quad (10)$$

More results on anomaly score functions are in Appendix C.

IV. MAIN EXPERIMENTS

In this section, we present our results for common unimodal and multimodal benchmarks, with a strong focus on the OE extension setting.

A. Implementation Details

We train our models using the objective function (7), where $\mathcal{L}_{\text{contrastive}}$ is SimCLR. We adopt ResNet-18 [15] as the main architecture, and we pre-train our models for 50 epochs using SimCLR. As for data augmentations T and T_{oe} , we follow the ones used by CSI [43]: namely, we apply random crop, horizontal flip, color jitter, and grayscale. If not mention otherwise, we detect OOD samples using the ensemble score function s_{μ} (10) with 32 augmentations.

In addition to the outlier-exposure extension, for unimodal benchmark, we also report the results using the fully self-supervised approach, where we train our models using the objective function (8) with CSI as $\mathcal{L}_{\text{contrastive}}$ and rotations as shifting transformations. Specifically, we choose $\mathcal{S} = \{\mathbb{I}, R_{90}\}$ and $\mathcal{S}_{\text{oe}} = \{R_{180}, R_{270}\}$, where R_a is the rotation of a° degree. Complete experimental details are available in the Appendix I.

B. Datasets

We evaluate our models using the standard CIFAR-10 [22] and ImageNet-30 [11, 18] datasets. We further conduct our experiments with additional datasets: the aerial dataset DIOR [25] and the microscopy dataset Raabin-WBC [21]. Both of them are symmetry datasets, which are obviously challenging for rotation-based methods like CSI [43], GT [18] or our self-OECL. It is important to clarify that, in this study, the term “non-standard” datasets refers to datasets from domains beyond conventional life photography.

For OE datasets, we use 80 Million Tiny Images (80MTI) [44] for the CIFAR-10 dataset and ImageNet-22k with ImageNet-1k removed for the other datasets. This follows the experimental setup in [18] and [29]. Please refer to the Appendix I for more details.

C. Benchmarks

We conduct our experiments in two main benchmarks: (1) unimodal and (2) multimodal benchmarks.

Unimodal benchmark. Generally, unimodal is the setting where there is one semantic class in the normal data. Within this study, if not mentioned otherwise, we mostly use the widely popular one vs. rest benchmark [37, 14, 17, 38, 43, 42, 10, 35, 9]. This benchmark is constructed based on classification datasets (e.g., CIFAR-10), where “one” class (e.g., “cat”) is considered normal and the “rest” classes (e.g., “dog”, “automobile”, ...) are considered anomalous during the test phase. Unless otherwise specified, we use all available classes as our one vs. rest classes.

Multimodal benchmark. We consider a recently and more challenging multimodal benchmark called leave-one-class-out [1, 29, 9]. In contrast to the one vs. rest benchmark, the roles are reversed, i.e., the “rest” classes (e.g., “dog”, “automobile”, ...) are designated as normal and the “one” class (e.g., “cat”) is abnormal. The presence of multiple semantically different classes as a normal class in this benchmark makes the distribution of normal samples multimodal [29], hence the models are required to learn high-quality deep representations to effectively distinguish between normal and abnormal samples. For all datasets, all available classes are employed as our leave-one-class-out classes. However, due to computational constraints, for ImageNet-30, we randomly select 10 classes as our leave-one-class-out classes. Additionally, when comparing the performance of OE-based methods, we also use unlabeled datasets as our normal datasets [43] (e.g., unlabeled CIFAR-10). The details are provided in the ??.

Throughout all of our experiments on the unimodal and multimodal benchmarks, we train our models using only the training data of the normal class and samples from an OE set that does not include any classes of the anomaly classes in the original classification datasets. We use the area under the receiver operating characteristic curve (AUC) to quantify detection performance.

D. Comparison Methods

End-to-end methods. We select methods that have demonstrated state-of-the-art performance on the CIFAR-10 and ImageNet-30 unimodal benchmarks. The unsupervised methods we consider include DSVDD [37], vanilla-SimCLR [43], GT+ [18], and CSI [43]. For unsupervised OE, we present the results from DSAD [38], HSC [29] and the unsupervised OE variant of GT+ [18]. For supervised OE, we use Focal [27] and BCE [29].

Transfer learning-based methods. We additionally explore transfer learning-based methods. For this category, we select the currently top-performing methods, which include DN2 [4], PANDA [35], Transformly [9], CLIP [34] and BCE-CL [29]. All methods are unsupervised with the exception of BCE-CL, which is a fine-tuned version of CLIP with a binary cross-entropy classifier.

The reported results were either extracted from the original papers, if available, or obtained by conducting experiments following the authors’s publicly available code (where possible).

E. Results and Analysis

Our main results are provided in Table I and Table II. Overall, our proposed methods achieve performance comparable to the current state-of-the-art methods and mostly outperform training-from-scratch approaches. A particularly surprising outcome is that our self-OECL surpasses CSI in the CIFAR-10 one vs. rest benchmark, while also obtaining decent performance in ImageNet-30. These results support our principles that enhancing the separation of normal and OOD samples in the contrastive feature space is beneficial for OOD detection. Furthermore, this property holds promising potential for future advancements in fully unsupervised OOD detection methods, particularly when more sophisticated OOD generation techniques are introduced (e.g., SDE-based methods [32]), transcending the limitations of rotations.

The benefits of OE datasets. Our OECL significantly enhances OOD detection compared to the baseline SimCLR in nearly all benchmarks, showcasing substantial improvements. The benefits of “anomalousness” from OE are especially evident for the unimodal non-standard datasets. Notably, the performance of CSI, a state-of-the-art non-OE method, as expected, shows minimal improvement and even degradation, with AUC scores of 78.5% for DIOR and 62.3% for Raabin-WBC, respectively. This is due to the fact that applying rotations no longer shifts the distribution of symmetry image datasets like DIOR and Raabin-WBC, which is the fundamental assumption of CSI. In contrast, the shift-distribution free OECL achieves higher scores of 91.1%(+12.6%) and 88.6%(+26.3%) for these datasets, which indicates the effectiveness of incorporating OE when working with non-standard datasets.

The power of contrastive learning. As reported in [29] and further supported by our experiments, there are situations where the current OE techniques struggle, such as the leave-one-class-out benchmark or non-standard training datasets. Particularly in the leave-one-class-out benchmark, where the training dataset’s distribution is multimodal, the strategy of encouraging the concentration of normal representations used in HSC [29] is ineffective, leading to suboptimal performance. Our proposed OECL, on the other hand, outperforms the majority of unsupervised methods in the multimodal setting, including those that used pre-trained features, as shown in Table II. Notably, OECL achieves a remarkable AUC score of 98.8% for the rich and diversified ImageNet-30, falling behind OE transfer learning-based BCE-CL by only 0.4%. These outcomes imply that, in contrast to HSC and BCE, the ability of OECL to exploit high-quality features through contrastive learning is especially advantageous in the context of multimodal datasets, particularly those that are rich and diverse standard datasets.

The necessity of training-from-scratch models. Surprisingly, the results on Raabin-WBC and multimodal DIOR show significant drops in performance for BCE-CL compared to our proposed OECL or SimCLR. This can be attributed to the fact that OECL is trained from scratch, whereas BCE-CL is fine-tuned over pre-training CLIP [34], which might not see many examples of (text, image) pairs for medical images along its training process. These results highlight the necessity of training-from-scratch models and raise concerns for the generalization of transfer learning in AD to specialize datasets.

Diminishing effect and settings where OE are less informa-

TABLE I: Mean AUC detection performance in % over 5 trials on the CIFAR-10, ImageNet-30, DIOR and Raabin-WBC in unimodal benchmarks. Bold denotes the best results for training-from-scratch methods, and underline denotes the overall best result. * denotes results taken from the reference, ‡ denotes results taken from [35]

Dataset	From scratch	Unsupervised					Unsupervised OE				Supervised OE		
		SimCLR	GT+	CSI	self-OECL	CLIP	GT+	DSAD	HSC	OECL	Focal	BCE	BCE-CL
	✓	✓	✓	✓	✓	✓	✓	✓	✓	✓	✓	✓	
CIFAR-10		86.1	90.1*	94.3*	94.7 ± 2.3	98.5	95.6*	94.5*	95.9*	97.8 ± 0.1	95.8*	96.1*	<u>99.6*</u>
ImageNet-30		64.8	84.8*	91.6*	87.3 ± 2.1	99.9	85.7*	96.7*	97.3*	97.7 ± 0.3	97.5*	97.7*	<u>99.9*</u>
DIOR		72.8	73.3‡	78.5‡	40.4 ± 6.8	87.3	79.3	88.3	89.2	91.1 ± 0.7	86.7	88.5	<u>97.7</u>
Raabin-WBC		85.9	73.6	62.3	62.1 ± 5.4	50.0	77.7	69.3	60.6	88.6 ± 1.9	68.9	66.5	51.0

TABLE II: Mean AUC detection performance in % over 2 trials on the CIFAR-10, ImageNet-30, DIOR and Raabin-WBC in multimodal benchmarks. Bold denotes the best results for training-from-scratch methods, and underline denotes the overall best result. * denotes results taken from the reference, ‡ denotes results taken from [9].

Dataset	From scratch	Unsupervised					Unsupervised OE		Supervised OE		
		DSVDD	SimCLR	DN2*	PANDA*	Transformly*	CLIP	HSC	OECL	BCE	BCE-CL
	✓	✓					✓	✓	✓		
CIFAR-10		50.7‡	83.9	71.7	78.5	90.4	92.2	84.8*	94.6 ± 0.6	86.6*	<u>98.4*</u>
ImageNet-30		×	94.8	×	×	×	97.7	86.7*	98.8 ± 0.1	86.5*	<u>99.2*</u>
DIOR		56.7‡	87.7	81.1	86.9	66.7	66.0	55.5	87.3 ± 1.9	62.5	61.4
Raabin-WBC		×	83.6	×	×	×	54.4	61.4	82.2 ± 3.3	62.1	61.3

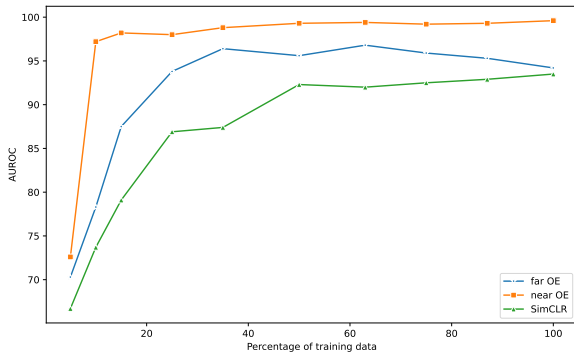


Fig. 3: AUROC scores across varying training data sizes for “near” and “far” OE datasets. The training dataset consists of lymphocyte and monocyte images, with eosinophil images from the Raabin-WBC dataset employed for testing. A combination of basophil and neutrophil images serves as the “near” OE, while ImageNet images serve as the “far” OE. As the training size increases, the influence of the “far” OE on anomaly detection diminishes, while “near” OE continues to synergize with the training data.

five. While it’s evident that OE datasets significantly contribute in improving anomaly detection in most of our experiments with OECL, their impact is minimal in the settings involving the multimodal non-standard datasets. This discrepancy may be attributed to the quality of deep features learned through $\mathcal{L}_{\text{contrastive}}$ and the relationship between OE datasets and training

datasets. Empirically, we observe that as the quality of learned features improves, OE datasets that are significantly different from the training distribution tend to have diminishing effects on AD performance, whereas OE datasets closer to the training distribution continue to enhance AD accuracy. We term this phenomenon the *diminishing effect* of OECL.

To demonstrate this, we conduct experiments using OECL with both “far” and “near” OE datasets on Raabin-WBC while gradually reducing the size of our training datasets. Given the difficulty in acquiring “near” OE data for Raabin-WBC, we designate subclasses basophil and neutrophil as “near” OE. We then train OECL on a combination of lymphocyte and monocyte images as normal data, with eosinophil images as testing data. For the “far” OE dataset, we again select ImageNet. The results in Figure 3 suggest that, as the quality of learned features from contrastive learning improves, the contribution of the “far” OE to anomaly detection diminishes, even though it significantly boosts anomaly detection performance when the learned features are of lower quality. In contrast, the features from the “near” OE dataset keep providing useful information to the model.

We also observed a more severe negative effect of “far” OE on the OE-based BCE-CL, which is a fine-tuned version of the sophisticated features-extractor CLIP [34, 29]. Using unlabeled CIFAR-10 as the normal dataset and CIFAR-100 as OOD images, we measure BCE-CL performances with OE datasets as 80MTI, SVHN [33], and DTD [8], respectively. Our results on Table III reveal that BCE-CL performances with 80MTI as OE easily achieves state-of-the-art results with an AUROC of 95.9%, a notable improvement over the the baseline

zero-shot CLIP with an AUROC of 90.8%. Conversely, when SVHN and DTD are used as OE datasets, the AUROC scores degrade to 62.8% and 60.5%, respectively. On the other hand, our proposed OECL achieves AUROC scores of 94.3% for 80MTI, 89.9% for SVHN, and 90.3% for DTD as OE datasets, significantly improving from the baseline SimCLR with an AUROC of 77.6%. These findings underscore the vulnerability of the state-of-the-art OE-based BCE-CL to “far” OE datasets, while demonstrating the robustness of OECL. Furthermore, these findings complement previous works [29], which suggest that the inclusion of OE transforms the anomaly detection problem into “a typical supervised classification problem that does not require a compact decision boundary”. Explicitly, the inclusion of OE requires a “sufficiently” compact decision boundary to achieve non-trivial AD performance.

TABLE III: AUC detection performance for BCE-CL and OECL with unlabeled CIFAR-10 as training dataset and CIFAR-100 as testing dataset.

Dataset	OE Dataset	CLIP	BCE-CL	SimCLR	OECL
Unlabeled CIFAR-10	80MTI		95.9		94.3
	SVHN	90.8	62.8	77.6	89.9
	DTD		60.5		90.3

Although our OECL proved its robustness, the above observations definitively highlight the necessity of carefully applying OE-based methods in real-life scenarios. More experiments and discussions over these phenomena are given in Appendix F and Appendix H.

V. APPLICABILITY OF OECL

A. Where and when to apply OECL

Scenarios where OECL fails. The results of self-OECL on two rotation-invariant datasets Raabin-WBC and DIOR point out an obvious vulnerability of our approach. When there’s substantial overlap between the training datasets and the OE datasets, directly minimizing the ℓ_2 -norm of contrastive features make our training process unstable, as shown in Figure 4, leading to the learning of trivial features. This observation emphasizes the importance of carefully considering the dataset characteristics when training OECL in practice.

Furthermore, another drawback of OECL is small training datasets. Given that OECL relies on contrastive representation learning to extract high-quality features, it struggles when confronted with datasets where $\mathcal{L}_{\text{contrastive}}$ module is unable to learn useful features and OE is not informative. OECL performances on small datasets such as MVTec-AD significantly lags behind specialized methods [3, 36] by a huge margin (+30%). Detailed experiments on small datasets are provided in Appendix D.

OECL as a robust, powerful and flexible tool for AD. OECL had prove its strength and robustness in a variety of settings and datasets. As a training-from-scratch model, OECL is viable in the cases where pre-trained network cannot be used. For example, when one must train a network from scratch due to architectural considerations (e.g., hardware constraints), or when there are security concerns regarding the white-box nature

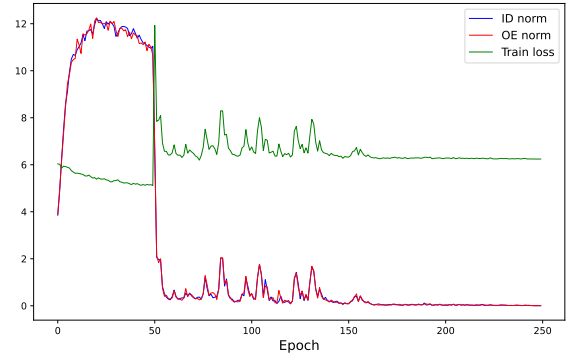


Fig. 4: The training loss and ℓ_2 -norm of ID and OE data when we train self-OECL on class monocyte of Raabin-WBC. When OE data and training data are overlap, directly minimizing ℓ_2 -norm of contrastive features makes the training becomes unstable and learns meaningless features (during the initial 50 epochs, we set $\alpha = 0$, more information about training is presented in Appendix G).

TABLE IV: Mean AUC detection performance in % of OECL over 5 trials on the Raabin-WBC and HAM1000 few-shot OOD benchmarks. Bold denotes the best results.

Normal Class	OE	Method	# Samples			
			k=0	k=1	k=10	Full-shot
Neutrophils	Lymphocytes	OECL	68.1	76.9	79.9	83.6
		BCE	×	49.0	72.6	95.0
		HSC	×	64.7	69.1	86.1
		BCE-CL	62.8	61.8	86.4	96.1
Melanocytic nevi	Melanoma	OECL	63.2	65.6	69.4	83.9
		BCE	×	61.7	60.4	79.1
		HSC	×	64.1	46.0	75.6
		BCE-CL	50.9	64.0	68.4	79.8
Melanocytic nevi	Benign keratosis	OECL	59.3	61.6	69.4	85.7
		BCE	×	53.2	54.3	84.8
		HSC	×	64.7	69.1	88.0
		BCE-CL	51.5	50.78	76.2	85.3

of pre-trained networks [39]. Additionally, the generalization of pre-trained models to specialize data, such as medical images, remains uncertain, underscoring the importance of training-from-scratch models in practical applications, as evidenced in Table I and Table II.

B. Few-shot OOD detection

We explore the generalization of OECL to unseen anomalies. In many real-life scenarios, we are able to collect some samples of a few specific classes of anomalies, which we term as “obtainable OOD classes”. For instance, in hematology, suppose that neutrophils, representing about 60% of circulating white blood cells, are regarded as normal samples, while white blood cells of other types are considered anomalies. Within this context, lymphocytes, which make up about 30% of white blood cells, can be considered an obtainable OOD class, and other white blood cells like basophils ($\approx 1\%$) and eosinophils ($\approx 3\%$) represent “unseen anomalies”.

Few-shot OOD benchmark. Inspired by [41] and [52], to evaluate OOD detection performance against unseen anomalies

described above, we introduce the “few-shot OOD” benchmark. This benchmark is constructed using classification datasets (e.g., Raabin-WBC), where the class with the largest number of samples (e.g., neutrophils) is considered as normal. The next largest class (e.g., lymphocytes) is selected as the obtainable OOD class, for which a small number of samples are available during training. All other classes (e.g., basophils, eosinophils, and monocytes) serve as unseen anomalies. At inference time, the goal is to identify normal samples and unseen abnormal samples. In this study, we focus on the extreme case one-shot and ten-shot detection, implying access to only a single sample and ten samples of obtainable OOD datasets, respectively ¹.

Datasets. In addition to the Raabin-WBC dataset, we use the HAM10000 dataset [45], which is a collection of dermatoscopic images of common pigmented skin lesions. Since the number of samples in the second and the third largest classes of HAM10000 are similar, we choose to do two experiments, where each of them serve as the obtainable OOD class.

Results and discussion. Results from Table IV show that exposing OECL to a small number of samples from a specific near-OOD class helps improve anomaly detection accuracy significantly. For less diverse Raabin-WBC, only one single OOD sample helps to boost the AUC score up about 9%. These results suggest a practical solution in which a limited number of OOD samples [24, 51] are integrated into the training phase to improve AD performance.

VI. CONCLUSION

We propose an easy-to-use but effective technique named outlier exposure contrastive learning, which extends the strengths of both contrastive learning and OE for out-of-distribution detection problems. OECL demonstrates strong and robust performance under various OOD detection scenarios. Additionally, we investigate scenarios where OE datasets might degrade the anomaly detection performance of OE-based methods. We believe that our work will serve as an essential baseline for future outlier exposure approaches to anomaly detection.

BROADER IMPACT

This study focuses on the domain of *out-of-distribution* (OOD) detection, which is a crucial part of trustworthy intelligent systems. Our research offers both theoretical and empirical findings regarding the behavior of ℓ_2 -norm in contrastive learning. Additionally, we propose a simple technique for directly incorporating OOD samples into contrastive learning methods. By leveraging “anomalousness” of OOD samples and high-quality representations of contrastive learning, our work will provide a feasible solution to problems where current OE and contrastive AD methods fail. We expect that these results will have an impact on real-life applications as well as academic advancements, leading to the development of safer and more dependable AI systems.

¹To some degree, the few-shot OOD benchmark represents unimodal benchmarks with very few standard OE samples.

REFERENCES

- [1] F. Ahmed and A. Courville. Detecting semantic anomalies. *Proceedings of the AAAI Conference on Artificial Intelligence*, 34(04):3154–3162, Apr. 2020. doi: 10.1609/aaai.v34i04.5712. URL <https://ojs.aaai.org/index.php/AAAI/article/view/5712>.
- [2] P. Bachman, R. D. Hjelm, and W. Buchwalter. *Learning Representations by Maximizing Mutual Information across Views*. Curran Associates Inc., Red Hook, NY, USA, 2019.
- [3] K. Batzner, L. Heckler, and R. König. Efficientad: Accurate visual anomaly detection at millisecond-level latencies, 2023.
- [4] L. Bergman, N. Cohen, and Y. Hoshen. Deep nearest neighbor anomaly detection. *CoRR*, abs/2002.10445, 2020. URL <https://arxiv.org/abs/2002.10445>.
- [5] P. Bergmann, M. Fauser, D. Sattlegger, and C. Steger. Mvtec ad — a comprehensive real-world dataset for unsupervised anomaly detection. In *2019 IEEE/CVF Conference on Computer Vision and Pattern Recognition (CVPR)*, pages 9584–9592, 2019. doi: 10.1109/CVPR.2019.00982.
- [6] D. Chen, S. Zhang, J. Yang, and B. Schiele. Norm-aware embedding for efficient person search. In *2020 IEEE/CVF Conference on Computer Vision and Pattern Recognition (CVPR)*, pages 12612–12621, 2020. doi: 10.1109/CVPR42600.2020.01263.
- [7] T. Chen, S. Kornblith, M. Norouzi, and G. Hinton. A simple framework for contrastive learning of visual representations. In H. D. III and A. Singh, editors, *Proceedings of the 37th International Conference on Machine Learning*, volume 119 of *Proceedings of Machine Learning Research*, pages 1597–1607. PMLR, 13–18 Jul 2020. URL <https://proceedings.mlr.press/v119/chen20j.html>.
- [8] M. Cimpoi, S. Maji, I. Kokkinos, S. Mohamed, and A. Vedaldi. Describing textures in the wild. In *2014 IEEE Conference on Computer Vision and Pattern Recognition*, pages 3606–3613, 2014. doi: 10.1109/CVPR.2014.461.
- [9] M. J. Cohen and S. Avidan. Transformally - two (feature spaces) are better than one. In *2022 IEEE/CVF Conference on Computer Vision and Pattern Recognition Workshops (CVPRW)*, pages 4059–4068, 2022. doi: 10.1109/CVPRW56347.2022.00451.
- [10] L. Deecke, L. Ruff, R. A. Vandermeulen, and H. Bilen. Transfer-based semantic anomaly detection. In M. Meila and T. Zhang, editors, *Proceedings of the 38th International Conference on Machine Learning*, volume 139 of *Proceedings of Machine Learning Research*, pages 2546–2558. PMLR, 18–24 Jul 2021. URL <https://proceedings.mlr.press/v139/deecke21a.html>.
- [11] J. Deng, W. Dong, R. Socher, L.-J. Li, K. Li, and L. Fei-Fei. Imagenet: A large-scale hierarchical image database. In *2009 IEEE Conference on Computer Vision and Pattern Recognition*, pages 248–255, 2009. doi: 10.1109/CVPR.2009.5206848.
- [12] A. Dosovitskiy, J. T. Springenberg, M. Riedmiller, and T. Brox. Discriminative unsupervised feature learning with convolutional neural networks. In Z. Ghahramani,

- M. Welling, C. Cortes, N. Lawrence, and K. Weinberger, editors, *Advances in Neural Information Processing Systems*, volume 27. Curran Associates, Inc., 2014. URL https://proceedings.neurips.cc/paper_files/paper/2014/file/07563a3fe3bbe7e3ba84431ad9d055af-Paper.pdf.
- [13] S. Gidaris, P. Singh, and N. Komodakis. Unsupervised representation learning by predicting image rotations. In *International Conference on Learning Representations*, 2018. URL <https://openreview.net/forum?id=S1v4N210->.
- [14] I. Golan and R. El-Yaniv. Deep anomaly detection using geometric transformations. In S. Bengio, H. Wallach, H. Larochelle, K. Grauman, N. Cesa-Bianchi, and R. Garnett, editors, *Advances in Neural Information Processing Systems*, volume 31. Curran Associates, Inc., 2018. URL https://proceedings.neurips.cc/paper_files/paper/2018/file/5e62d03aec0d17facfc5355dd90d441c-Paper.pdf.
- [15] K. He, X. Zhang, S. Ren, and J. Sun. Deep residual learning for image recognition. In *2016 IEEE Conference on Computer Vision and Pattern Recognition (CVPR)*, pages 770–778, 2016. doi: 10.1109/CVPR.2016.90.
- [16] K. He, H. Fan, Y. Wu, S. Xie, and R. Girshick. Momentum contrast for unsupervised visual representation learning. In *2020 IEEE/CVF Conference on Computer Vision and Pattern Recognition (CVPR)*, pages 9726–9735, 2020. doi: 10.1109/CVPR42600.2020.00975.
- [17] D. Hendrycks, M. Mazeika, and T. Dietterich. Deep anomaly detection with outlier exposure. In *International Conference on Learning Representations*, 2019. URL <https://openreview.net/forum?id=HyxCxhRcY7>.
- [18] D. Hendrycks, M. Mazeika, S. Kadavath, and D. Song. Using self-supervised learning can improve model robustness and uncertainty. In H. Wallach, H. Larochelle, A. Beygelzimer, F. d’Alché-Buc, E. Fox, and R. Garnett, editors, *Advances in Neural Information Processing Systems*, volume 32. Curran Associates, Inc., 2019. URL https://proceedings.neurips.cc/paper_files/paper/2019/file/a2b15837edac15df90721968986f7f8e-Paper.pdf.
- [19] S. Ioffe and C. Szegedy. Batch normalization: Accelerating deep network training by reducing internal covariate shift. In F. Bach and D. Blei, editors, *Proceedings of the 32nd International Conference on Machine Learning*, volume 37 of *Proceedings of Machine Learning Research*, pages 448–456, Lille, France, 07–09 Jul 2015. PMLR. URL <https://proceedings.mlr.press/v37/ioffe15.html>.
- [20] P. Khosla, P. Teterwak, C. Wang, A. Sarna, Y. Tian, P. Isola, A. Maschinot, C. Liu, and D. Krishnan. Supervised contrastive learning. In *Proceedings of the 34th International Conference on Neural Information Processing Systems*, NIPS’20, Red Hook, NY, USA, 2020. Curran Associates Inc. ISBN 9781713829546.
- [21] Z. M. Kouzehkanan, S. Saghari, S. Tavakoli, P. Rostami, M. Abaszadeh, F. Mirzadeh, E. S. Satlsar, M. Gheidshahran, F. Gorgi, S. Mohammadi, and R. Hosseini. A large dataset of white blood cells containing cell locations and types, along with segmented nuclei and cytoplasm. *Scientific Reports*, 12(1):1123, 2022. doi: 10.1038/s41598-021-04426-x. URL <https://doi.org/10.1038/s41598-021-04426-x>.
- [22] A. Krizhevsky. Learning multiple layers of features from tiny images. 2009.
- [23] C.-L. Li, K. Sohn, J. Yoon, and T. Pfister. Cutpaste: Self-supervised learning for anomaly detection and localization. In *2021 IEEE/CVF Conference on Computer Vision and Pattern Recognition (CVPR)*, pages 9659–9669, 2021. doi: 10.1109/CVPR46437.2021.00954.
- [24] C.-L. Li, K. Sohn, J. Yoon, and T. Pfister. Cutpaste: Self-supervised learning for anomaly detection and localization. In *Proceedings of the IEEE/CVF conference on computer vision and pattern recognition*, pages 9664–9674, 2021.
- [25] K. Li, G. Wan, G. Cheng, L. Meng, and J. Han. Object detection in optical remote sensing images: A survey and a new benchmark. *ISPRS Journal of Photogrammetry and Remote Sensing*, 159:296–307, 2020. ISSN 0924-2716. doi: <https://doi.org/10.1016/j.isprsjprs.2019.11.023>. URL <https://www.sciencedirect.com/science/article/pii/S0924271619302825>.
- [26] X. Li, Z. Huang, F. Xue, and Y. Zhou. Musc: Zero-shot industrial anomaly classification and segmentation with mutual scoring of the unlabeled images. In *International Conference on Learning Representations*, 2024.
- [27] T.-Y. Lin, P. Goyal, R. Girshick, K. He, and P. Dollár. Focal loss for dense object detection. In *2017 IEEE International Conference on Computer Vision (ICCV)*, pages 2999–3007, 2017. doi: 10.1109/ICCV.2017.324.
- [28] Z. Liu, Y. Zhou, Y. Xu, and Z. Wang. Simplenet: A simple network for image anomaly detection and localization. In *Proceedings of the IEEE/CVF Conference on Computer Vision and Pattern Recognition*, pages 20402–20411, 2023.
- [29] P. Liznerski, L. Ruff, R. A. Vandermeulen, B. J. Franks, K. R. Muller, and M. Kloft. Exposing outlier exposure: What can be learned from few, one, and zero outlier images. *Transactions on Machine Learning Research*, 2022. ISSN 2835-8856. URL <https://openreview.net/forum?id=3v78awEzyB>.
- [30] I. Loshchilov and F. Hutter. SGDR: stochastic gradient descent with restarts. *CoRR*, abs/1608.03983, 2016. URL <http://arxiv.org/abs/1608.03983>.
- [31] Q. Meng, S. Zhao, Z. Huang, and F. Zhou. Magface: A universal representation for face recognition and quality assessment. In *2021 IEEE/CVF Conference on Computer Vision and Pattern Recognition (CVPR)*, pages 14220–14229, 2021. doi: 10.1109/CVPR46437.2021.01400.
- [32] H. Mirzaei, M. Salehi, S. Shahabi, E. Gavves, C. G. M. Snoek, M. Sabokrou, and M. H. Rohban. Fake it until you make it : Towards accurate near-distribution novelty detection. In *NeurIPS ML Safety Workshop*, 2022. URL <https://openreview.net/forum?id=zNlvtJnoPY2>.
- [33] Y. Netzer, T. Wang, A. Coates, A. Bissacco, B. Wu, and A. Y. Ng. Reading digits in natural images with unsupervised feature learning. 2011. URL http://ufldl.stanford.edu/housenumbers/nips2011_housenumbers.pdf.
- [34] A. Radford, J. W. Kim, C. Hallacy, A. Ramesh, G. Goh, S. Agarwal, G. Sastry, A. Askell, P. Mishkin, J. Clark, G. Krueger, and I. Sutskever. Learning transferable

- visual models from natural language supervision. In M. Meila and T. Zhang, editors, *Proceedings of the 38th International Conference on Machine Learning*, volume 139 of *Proceedings of Machine Learning Research*, pages 8748–8763. PMLR, 18–24 Jul 2021. URL <https://proceedings.mlr.press/v139/radford21a.html>.
- [35] T. Reiss, N. Cohen, L. Bergman, and Y. Hoshen. Panda: Adapting pretrained features for anomaly detection and segmentation. In *Proceedings of the IEEE/CVF Conference on Computer Vision and Pattern Recognition*, pages 2806–2814, 2021.
- [36] K. Roth, L. Pemula, J. Zepeda, B. Schölkopf, T. Brox, and P. Gehler. Towards total recall in industrial anomaly detection. In *2022 IEEE/CVF Conference on Computer Vision and Pattern Recognition (CVPR)*, pages 14298–14308, 2022. doi: 10.1109/CVPR52688.2022.01392.
- [37] L. Ruff, R. Vandermeulen, N. Goernitz, L. Deecke, S. A. Siddiqui, A. Binder, E. Müller, and M. Kloft. Deep one-class classification. In J. Dy and A. Krause, editors, *Proceedings of the 35th International Conference on Machine Learning*, volume 80 of *Proceedings of Machine Learning Research*, pages 4393–4402. PMLR, 10–15 Jul 2018. URL <https://proceedings.mlr.press/v80/ruff18a.html>.
- [38] L. Ruff, R. A. Vandermeulen, N. Görnitz, A. Binder, E. Müller, K.-R. Müller, and M. Kloft. Deep semi-supervised anomaly detection. In *International Conference on Learning Representations*, 2020. URL <https://openreview.net/forum?id=HkgH0TEYwH>.
- [39] W. Samek, G. Montavon, S. Lapuschkin, C. J. Anders, and K.-R. Müller. Explaining deep neural networks and beyond: A review of methods and applications. *Proceedings of the IEEE*, 109(3):247–278, 2021. doi: 10.1109/JPROC.2021.3060483.
- [40] H. M. Schlüter, J. Tan, B. Hou, and B. Kainz. Natural synthetic anomalies for self-supervised anomaly detection and localization. In *European Conference on Computer Vision*, pages 474–489. Springer, 2022.
- [41] V. Sehwag, M. Chiang, and P. Mittal. Ssd: A unified framework for self-supervised outlier detection. In *International Conference on Learning Representations*, 2021. URL <https://openreview.net/forum?id=v5gjXpmR8J>.
- [42] K. Sohn, C.-L. Li, J. Yoon, M. Jin, and T. Pfister. Learning and evaluating representations for deep one-class classification. In *International Conference on Learning Representations*, 2021. URL <https://openreview.net/forum?id=HCSgyPUfeDj>.
- [43] J. Tack, S. Mo, J. Jeong, and J. Shin. Csi: Novelty detection via contrastive learning on distributionally shifted instances. In H. Larochelle, M. Ranzato, R. Hadsell, M. Balcan, and H. Lin, editors, *Advances in Neural Information Processing Systems*, volume 33, pages 11839–11852. Curran Associates, Inc., 2020. URL https://proceedings.neurips.cc/paper_files/paper/2020/file/8965f76632d7672e7d3cf29c87ecaa0c-Paper.pdf.
- [44] A. Torralba, R. Fergus, and W. T. Freeman. 80 million tiny images: A large data set for nonparametric object and scene recognition. *IEEE Transactions on Pattern Analysis and Machine Intelligence*, 30(11):1958–1970, 2008. doi: 10.1109/TPAMI.2008.128.
- [45] P. Tschandl. The HAM10000 dataset, a large collection of multi-source dermatoscopic images of common pigmented skin lesions, 2018. URL <https://doi.org/10.7910/DVN/DBW86T>.
- [46] S. Vaze, K. Han, A. Vedaldi, and A. Zisserman. Open-set recognition: a good closed-set classifier is all you need? In *International Conference on Learning Representations*, 2022.
- [47] S. Wang, Y. Zeng, X. Liu, E. Zhu, J. Yin, C. Xu, and M. Kloft. Effective end-to-end unsupervised outlier detection via inlier priority of discriminative network. In H. Wallach, H. Larochelle, A. Beygelzimer, F. d'Alché-Buc, E. Fox, and R. Garnett, editors, *Advances in Neural Information Processing Systems*, volume 32. Curran Associates, Inc., 2019. URL https://proceedings.neurips.cc/paper_files/paper/2019/file/6c4bb406b3e7cd5447f7a76fd7008806-Paper.pdf.
- [48] T. Wang and P. Isola. Understanding contrastive representation learning through alignment and uniformity on the hypersphere. In H. D. III and A. Singh, editors, *Proceedings of the 37th International Conference on Machine Learning*, volume 119 of *Proceedings of Machine Learning Research*, pages 9929–9939. PMLR, 13–18 Jul 2020. URL <https://proceedings.mlr.press/v119/wang20k.html>.
- [49] Y. You, I. Gitman, and B. Ginsburg. Scaling SGD batch size to 32k for imagenet training. *CoRR*, abs/1708.03888, 2017. URL <http://arxiv.org/abs/1708.03888>.
- [50] C. Yu, X. Zhu, Z. Lei, and S. Z. Li. Out-of-distribution detection for reliable face recognition. *IEEE Signal Processing Letters*, 27:710–714, 2020. doi: 10.1109/LSP.2020.2988140.
- [51] V. Zavrtnik, M. Kristan, and D. Skocaj. Draem - a discriminatively trained reconstruction embedding for surface anomaly detection. In *Proceedings of the IEEE/CVF International Conference on Computer Vision (ICCV)*, pages 8330–8339, October 2021.
- [52] Z. Zhou, L.-Z. Guo, Z. Cheng, Y.-F. Li, and S. Pu. Step: Out-of-distribution detection in the presence of limited in-distribution labeled data. In M. Ranzato, A. Beygelzimer, Y. Dauphin, P. Liang, and J. W. Vaughan, editors, *Advances in Neural Information Processing Systems*, volume 34, pages 29168–29180. Curran Associates, Inc., 2021. URL https://proceedings.neurips.cc/paper_files/paper/2021/file/f4334c131c781e2a6f0a5e34814c8147-Paper.pdf.

APPENDIX

A. Proof of Theorem III.1

Lemma A.1. For any $\mu > 0$, $f(y)$ is a non-increasing and convex function on $[0, \infty)$ where

$$f(y) = \int_{-\infty}^{\infty} \frac{x}{\sqrt{x^2 + y}} e^{-(x-\mu)^2/2\sigma^2} dx$$

Proof. Firstly, rewrite

$$\begin{aligned} f(y) &= \int_0^{\infty} + \int_{-\infty}^0 \frac{x}{\sqrt{x^2 + y}} e^{-(x-\mu)^2/2\sigma^2} dx \\ &= \int_0^{\infty} \frac{x}{\sqrt{x^2 + y}} \left(e^{-(x-\mu)^2/2\sigma^2} - e^{-(x+\mu)^2/2\sigma^2} \right) dx \\ &= \int_0^{\infty} \frac{x}{\sqrt{x^2 + y}} e^{-(x+\mu)^2/2\sigma^2} \left(e^{2x\mu/\sigma^2} - 1 \right) dx \end{aligned}$$

$f'(y)$ and $f''(y)$ given by

$$\begin{aligned} f'(y) &= \left(\int_0^{\infty} \frac{x}{\sqrt{x^2 + y}} e^{-(x+\mu)^2/2\sigma^2} \left(e^{2x\mu/\sigma^2} - 1 \right) dx \right)'_y \\ &= \int_0^{\infty} \left(\frac{x}{\sqrt{x^2 + y}} \right)'_y e^{-(x+\mu)^2/2\sigma^2} \left(e^{2x\mu/\sigma^2} - 1 \right) dx \\ &= \int_0^{\infty} \frac{-x}{2(x^2 + y)^{3/2}} e^{-(x+\mu)^2/2\sigma^2} \left(e^{2x\mu/\sigma^2} - 1 \right) dx \\ f''(y) &= \left(\int_0^{\infty} \frac{x}{\sqrt{x^2 + y}} e^{-(x+\mu)^2/2\sigma^2} \left(e^{2x\mu/\sigma^2} - 1 \right) dx \right)''_y \\ &= \int_0^{\infty} \left(\frac{x}{\sqrt{x^2 + y}} \right)''_y e^{-(x+\mu)^2/2\sigma^2} \left(e^{2x\mu/\sigma^2} - 1 \right) dx \\ &= \int_0^{\infty} \frac{3x}{(x^2 + y)^{5/2}} e^{-(x+\mu)^2/2\sigma^2} \left(e^{2x\mu/\sigma^2} - 1 \right) dx \end{aligned}$$

Since $e^{2x\mu/\sigma^2} \geq 1 \forall x > 0$, it's clear that $f'(y) < 0$ and $f''(y) > 0$, i.e, $f(y)$ is non-increase and convex over $[0, \infty)$. \square

Theorem III.1. Given two vectors $\mathbf{X} = (X_1, X_2, \dots, X_n)^t$ and $\mathbf{Y} = (Y_1, Y_2, \dots, Y_n)^t$ are i.i.d $\mathcal{N}(\mu, \Sigma)$ where $\mu = (\mu, 0, \dots, 0)^t$, $\mu \geq 0$ and $\Sigma = \begin{bmatrix} \sigma & \mathbf{0} \\ \mathbf{0} & \Sigma_V \end{bmatrix}$. Then,

- 1) $\mathbb{E} \left\langle \frac{\mathbf{X}}{\|\mathbf{X}\|}, \frac{\mathbf{Y}}{\|\mathbf{Y}\|} \right\rangle$ is an increasing function of μ
- 2) The following inequalities hold for all $\epsilon > 0$

$$\mathbb{E} \left\langle \frac{\mathbf{X}}{\|\mathbf{X}\|}, \frac{\mathbf{Y}}{\|\mathbf{Y}\|} \right\rangle \leq \left(\Phi \left(\frac{\mu}{\sigma} \right) - \Phi \left(-\frac{\mu}{\sigma} \right) \right)^2, \quad (5)$$

$$\begin{aligned} \mathbb{E} \left\langle \frac{\mathbf{X}}{\|\mathbf{X}\|}, \frac{\mathbf{Y}}{\|\mathbf{Y}\|} \right\rangle &\geq \\ &\frac{1}{1 + \frac{\sigma_V^2}{\epsilon^2 \mu^2}} \left(\Phi \left(\frac{(1-\epsilon)\mu}{\sigma} \right) - \Phi \left(\frac{-(1+\epsilon)\mu}{\sigma} \right) \right)^2, \quad (6) \end{aligned}$$

where $\sigma_V^2 = \text{tr}(\Sigma_V)$ and Φ is the cumulative distribution function of $\mathcal{N}(0, 1)$.

Proof of Theorem III.1. Since $EX_i = 0$ for $i \geq 2$ and they are jointly normal distribution, we have

$$\mathbb{E} \frac{X_i}{\sqrt{X_1^2 + X_2^2 + \dots + X_n^2}} = 0 \quad \forall i \in \{2, \dots, n\}.$$

Hence,

$$\mathbb{E} \left\langle \frac{\mathbf{X}}{\|\mathbf{X}\|}, \frac{\mathbf{Y}}{\|\mathbf{Y}\|} \right\rangle = \mathbb{E} \frac{X_1 Y_1}{\|\mathbf{X}\| \|\mathbf{Y}\|} + \sum_{i=2}^n \mathbb{E} \frac{X_i Y_i}{\|\mathbf{X}\| \|\mathbf{Y}\|} = \left(\mathbb{E} \left[\frac{X_1}{\|\mathbf{X}\|} \right] \right)^2$$

Let denote $U = X_1$, $V = (X_2, \dots, X_n)^t$ and $Z = \|V\|_2^2 = \sum_{i=2}^n X_i^2$. The expectation of cosine similarity between two vectors \mathbf{X} and \mathbf{Y} becomes

$$\left(\frac{1}{\sigma\sqrt{2\pi}} \int_{-\infty}^{\infty} \frac{u}{\sqrt{u^2+z}} e^{-(u-\mu)^2/2\sigma^2} du \int_0^{\infty} f_Z(z) dz \right)^2,$$

where f_Z are probability density function of Z .

1) Let

$$A = \frac{1}{\sigma\sqrt{2\pi}} \int_{-\infty}^{\infty} \frac{u}{\sqrt{u^2+z}} e^{-(u-\mu)^2/2\sigma^2} du \int_0^{\infty} f_Z(z) dz.$$

By the change of variable theorem, replacing $u = u + \mu$ give

$$A = \frac{1}{\sigma\sqrt{2\pi}} \int_{-\infty}^{\infty} \frac{u+\mu}{\sqrt{(u+\mu)^2+z}} e^{-u^2/2\sigma^2} du \int_0^{\infty} f_Z(z) dz$$

Get derivative,

$$A'_\mu = \frac{1}{\sigma\sqrt{2\pi}} \int_{-\infty}^{\infty} \frac{z}{\sqrt{((u+\mu)^2+z)^3}} e^{-u^2/2\sigma^2} du \int_0^{\infty} f_Z(z) dz > 0$$

2) For (5), using Lemma A.1 we have $f(z) = \int_{-\infty}^{\infty} \frac{u}{\sqrt{u^2+z}} e^{-(u-\mu)^2/2\sigma^2} du$ is an decreasing function on $[0, \infty)$, thus $f(z) \leq f(0) \forall z \geq 0$. This gives us

$$\begin{aligned} A &= \frac{1}{\sigma\sqrt{2\pi}} \int_{-\infty}^{\infty} \frac{u}{\sqrt{u^2+z}} e^{-(u-\mu)^2/2\sigma^2} du \int_0^{\infty} f_Z(z) dz \\ &\leq \left(\frac{1}{\sigma\sqrt{2\pi}} \int_{-\infty}^{\infty} \frac{u}{|u|} e^{-(u-\mu)^2/2\sigma^2} du \right) \left(\int_0^{\infty} f_Z(z) dz \right) \\ &= \frac{1}{\sigma\sqrt{2\pi}} \left(\int_0^{\infty} e^{-(u-\mu)^2/2\sigma^2} du - \int_{-\infty}^0 e^{-(u-\mu)^2/2\sigma^2} du \right) \\ &= \frac{1}{\sqrt{2\pi}} \left(\int_{-\mu/\sigma}^{\infty} e^{-u^2/2} du - \int_{-\infty}^{-\mu/\sigma} e^{-u^2/2} du \right) \\ &= \Phi\left(\frac{\mu}{\sigma}\right) - \Phi\left(-\frac{\mu}{\sigma}\right) \end{aligned}$$

For (6), we have $f(z)$ is convex by Lemma A.1. Jensen's inequality gives us

$$A = \frac{1}{\sigma\sqrt{2\pi}} \mathbb{E}_Z f(Z) \geq \frac{1}{\sigma\sqrt{2\pi}} f(\mathbb{E}_Z(Z)).$$

Since $\mathbb{E}Z = \mathbb{E}[\sum_{i=2}^n X_i^2] = \sum_{i=2}^n \mathbb{E}X_i^2 = \text{tr}(\Sigma_V) = \sigma_V^2$, thus

$$\begin{aligned} A &\geq \frac{1}{\sigma\sqrt{2\pi}} \int_{-\infty}^{\infty} \frac{u}{\sqrt{u^2+\sigma_V^2}} e^{-(u-\mu)^2/2\sigma^2} du \\ &= \frac{1}{\sigma\sqrt{2\pi}} \int_0^{\infty} \frac{u}{\sqrt{u^2+\sigma_V^2}} \left(e^{-(u-\mu)^2/2\sigma^2} - e^{-(u+\mu)^2/2\sigma^2} \right) du \\ &> \frac{1}{\sigma\sqrt{2\pi}} \int_{\epsilon\mu}^{\infty} \frac{u}{\sqrt{u^2+\sigma_V^2}} \left(e^{-(u-\mu)^2/2\sigma^2} - e^{-(u+\mu)^2/2\sigma^2} \right) du \quad \forall \epsilon > 0 \\ &\geq \frac{1}{\sigma\sqrt{2\pi}} \left(\frac{\epsilon\mu}{\sqrt{(\epsilon\mu)^2+\sigma_V^2}} \int_{\epsilon\mu}^{\infty} \left(e^{-(u-\mu)^2/2\sigma^2} - e^{-(u+\mu)^2/2\sigma^2} \right) du \right) \\ &= \frac{1}{\sqrt{1+\frac{\sigma_V^2}{\epsilon^2\mu^2}}} \frac{1}{\sqrt{2\pi}} \left(\int_{(\epsilon-1)\mu/\sigma}^{\infty} e^{-u^2/2} du - \int_{(\epsilon+1)\mu/\sigma}^{\infty} e^{-u^2/2} du \right) \\ &= \frac{1}{\sqrt{1+\frac{\sigma_V^2}{\epsilon^2\mu^2}}} \left(\Phi\left(\frac{(1-\epsilon)\mu}{\sigma}\right) - \Phi\left(-\frac{(1+\epsilon)\mu}{\sigma}\right) \right) \end{aligned} \tag{11}$$

The Equation (11) is due to the fact that $\frac{u}{\sqrt{u^2+\sigma_V^2}}$ is an increasing function in u .

□

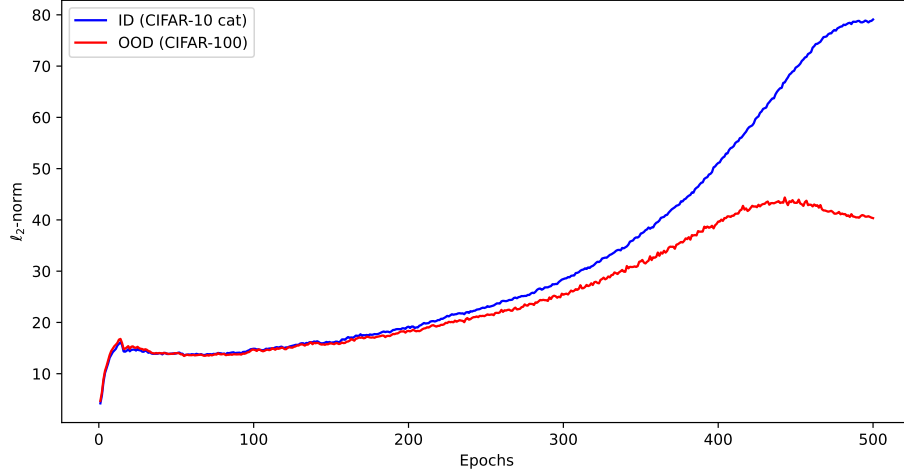


Fig. 5: ℓ_2 -norm of contrastive features for both normal and OOD samples during optimization of $\mathcal{L}_{\text{contrastive}}$ without ℓ_2 -normalization, using only normal samples.

B. Gradual reduction of the ℓ_2 -norm of contrastive features

In this section, to study the effect of *alignment* and *uniformity* on the ℓ_2 -norm of contrastive features, we use the contrastive learning framework proposed by [48],

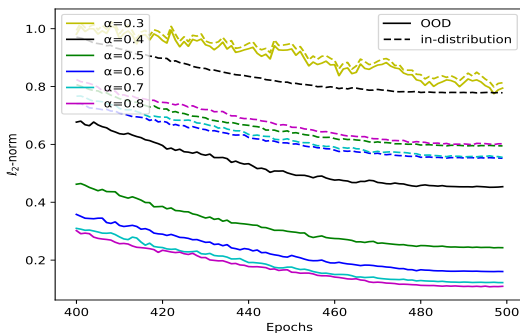
$$\mathcal{L}_{\text{contrastive}} = \mathcal{L}_{\text{align}} + \mathcal{L}_{\text{uniform}},$$

where

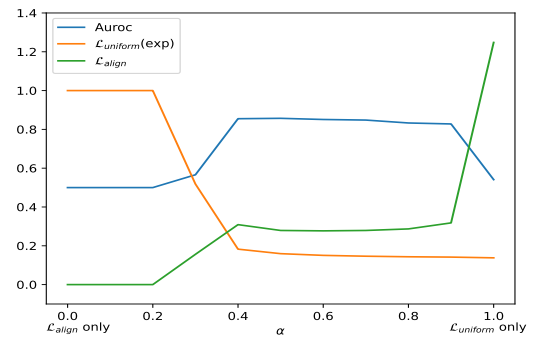
$$\mathcal{L}_{\text{align}} = \mathbb{E}_{(x,y) \sim p_{\text{pos}}} [\|z(x) - z(y)\|_2^2], \quad (12)$$

$$\mathcal{L}_{\text{uniform}} = \log \mathbb{E}_{(x,y) \stackrel{\text{i.i.d.}}{\sim} p_{\text{data}}} [e^{-\|z(x) - z(y)\|_2^2}]. \quad (13)$$

Necessity of cosine similarity. Figure 5 depicts the ℓ_2 -norm of contrastive features during optimization of $\mathcal{L}_{\text{contrastive}}$ using Euclidean distance, i.e., $z(x) = f(x)$. As expected, without ℓ_2 -normalization, the ℓ_2 -norm of contrastive features $f(x)$ does not exhibit the characteristic of gradual decrease but rather increases as training progresses. This shows the critical role played by cosine similarity in driving the gradual reduction of the ℓ_2 -norm of contrastive features.



(a) ℓ_2 -norm of contrastive features.



(b) $\mathcal{L}_{\text{align}}$, $\mathcal{L}_{\text{uniform}}$ and AUC score.

Fig. 6: Impact of optimizing different weighted combinations of $\mathcal{L}_{\text{align}}$ and $\mathcal{L}_{\text{uniform}}$, trained on CIFAR-10 cat class. $\mathcal{L}_{\text{uniform}}$ is exponentiated for visualization.

Necessity of both alignment and uniformity. Figure 6 shows how the AUC score and the ℓ_2 -norm change in response to optimizing differently weighted combinations $(1 - \alpha)\mathcal{L}_{\text{align}} + \alpha\mathcal{L}_{\text{uniform}}$. Similar to the accuracy curve in [48], AUC score curve of OOD detection is also inverted-U-shaped. This means that both *alignment* and *uniformity* are vital for a high-quality features extractor, hence is necessity for a good OOD detector. When $\mathcal{L}_{\text{align}}$ is weighted much higher than $\mathcal{L}_{\text{uniform}}$, degenerate solution occurs and all inputs (including normal and OOD samples) are mapped to the same point ($\exp(\mathcal{L}_{\text{uniform}})=1$). However, as long as the ratio between two weights is not too large (e.g., $0.4 \leq \alpha \leq 0.9$), we consistently observe both the gap between the ℓ_2 -norm of normal and OOD contrastive representations and their gradual reduction as training progresses. An intriguing observation is the relation between α and the ℓ_2 -norm of OOD samples; as the value of α increases, the ℓ_2 -norm of OOD contrastive features decreases proportionally. This suggests that uniformity plays a more significant role in the gradual reduction of ℓ_2 -norm of contrastive features. We hope that future research will offer a more in-depth understanding of the fundamental cause of this phenomenon.

C. Anomaly detection scores

We consider the following anomaly detection scores,

$$s_{\ell_2} = \|f(x)\|_2^2 \quad (14)$$

$$s_{\ell_2-\text{ens}} = \mathbb{E}_{t \in T} \|f(t(x))\|_2^2 = \mu^2 + \sigma^2 + \sigma_V^2 \quad (15)$$

$$s_{\mu} = \|\mathbb{E}_{t \in T} f(t(x))\|_2^2 = \mu^2 \quad (16)$$

Experimentally, we find that the overall detection performance of s_{μ} is better, especially for non-standard datasets as shown in Table V.

TABLE V: AUC detection performance in % using s_{ℓ_2} , $s_{\ell_2-\text{ens}}$ and s_{μ} .

Dataset	Benchmark	s_{μ}	$s_{\ell_2-\text{ens}}$	s_{ℓ_2}
DIOR	unimodal	91.1	90.7	90.8
	multimodal	87.3	86.9	87.1
Raabin-WBC	unimodal	88.6	88.4	88.6
	multimodal	82.2	82.0	81.4
CIFAR-10	unimodal	97.8	97.5	96.4
	multimodal	94.6	94.4	93.8
ImageNet-30	unimodal	97.7	97.7	95.9
	multimodal	98.8	98.8	97.8

Another potential addition to the anomaly scores involves incorporating the cosine similarity to the nearest sample as suggested in [43]. While we have observed a similar phenomenon in our experiments, where the combination of cosine similarity and feature norm mostly yields the best results, it may not exhibit absolute consistency across various scenarios, as indicated in Table VI. Furthermore, we wish to emphasize the effectiveness of the ℓ_2 -norm in anomaly detection. Therefore, we have chosen to present our anomaly score without the inclusion of cosine similarity.

TABLE VI: AUC detection performance in % using s_{μ} and $\text{sim} + s_{\mu}$.

Dataset	Benchmark	OE	s_{μ}	$\text{sim} + s_{\mu}$
Raabin-WBC	unimodal		85.9	88.1
Raabin-WBC	unimodal	✓	88.6	89.0
DIOR	unimodal		72.8	74.9
DIOR	unimodal	✓	91.1	91.2
CIFAR-10	unimodal		86.1	86.8
CIFAR-10	unimodal	✓	97.8	97.7
ImageNet-30	unimodal		64.8	66.7
ImageNet-30	unimodal	✓	97.7	97.5

D. Small datasets

Due to the fact that OECL relies on contrastive representation learning to extract high-quality features, it does not perform well on datasets where its contrastive learning module is unable to learn strong features and OE is not informative. This is particularly evident in scenarios where the training datasets are small and non-standard. To illustrate this, we use the DTD [8] one vs. rest benchmark and the recent manufacturing dataset MVTec-AD [5], with ImageNet22k serving as the OE dataset.

DTD is a dataset that includes different classes of textures. Comprising 15 distinct classes of manufacturing objects (such as screws, cables, and capsules), MVTec-AD presents both normal and abnormal samples for each class. For example, a screw

class consists of two sets of images: a training set of images of typical screws, and a test set of images of typical screws, along with images of screws with anomalous defects. Both DTD and MVtec-AD consist of fewer than 40 samples for each normal class. Table VII shows the results of OECL on these small datasets.

TABLE VII: Mean AUC detection performance in % over 5 trials on the DTD one vs. rest and on the MVTec-AD benchmarks with ImageNet1k OE.

Dataset	OECL	HSC*	BCE*	Patchcore	EfficientAD
DTD	65.6	72.7	73.3	×	×
MVTec-AD	62.1	70.1	66.1	99.1	99.1

As anticipated, OECL results more poorly on the small datasets than state-of-the-art methods: OECL scores around 62% while [3] and [36] score above 99% AUC for the MVTec-AD benchmark. These results indicate that for small datasets, OECL may not be the optimal choice.

E. OECL with SupCLR

In this subsection, we present the OECL version of SupCLR [20]. Instead of using SimCLR for $\mathcal{L}_{\text{contrastive}}$ in Equation (7), we utilize SupCLR. SupCLR is a supervised extension of SimCLR that contrasts samples *class-wise*. Hence, we conduct our experiments using labeled CIFAR-10 with the OE dataset is 80MTI, and the out-of-distribution (OOD) data are common benchmark datasets: CIFAR-100 and SVHN. For comparison, we also include experiments using OECL on unlabeled CIFAR-10. The results show that OE can improve the performance of SupCLR on anomaly detection.

TABLE VIII: AUC detection performance of SupCLR and its OE extension on CIFAR-10.

Dataset	Method	OOD Dataset	
		CIFAR-100	SVHN
Labeled CIFAR-10	SupCLR	88.6	97.3
	OE + SupCLR	95.2	97.4
Unlabeled CIFAR-10	OECL	94.3	99.4

F. The diminishing effect.

We provide results for unlabelled CIFAR-10 datasets in Figure 7. The test data is CIFAR-100 and we choose SVHN as “far” OE and keep using 80MTI as “near” OE dataset.

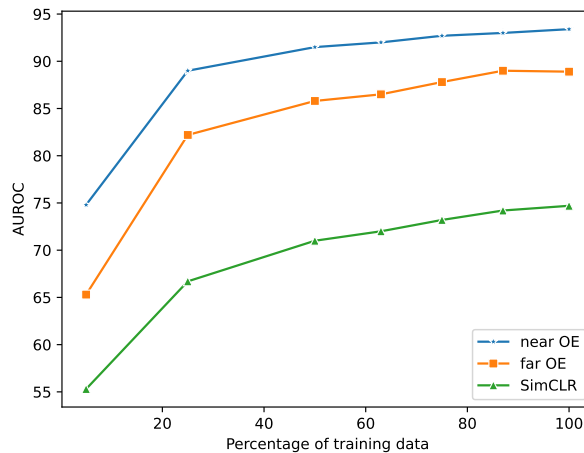


Fig. 7: AUROC scores across varying training data sizes for “near” and “far” OE datasets. The training dataset is unlabeled CIFAR-10. The test data is CIFAR-100 and we choose SVHN as “far” OE and keep using 80MTI as “near” OE dataset.

G. Warm-up with SimCLR

As mentioned in Section V-A, brutally force ℓ_2 -norm of OE samples to zero may cause the instability in training process, especially when OE samples might overlap with training dataset. Since SimCLR uses hard augmentations, for example, CSI [43] uses RandomResizeCrop with scale uniformly from 0.08 up to 1, augmentations of training samples and OE samples might send wrong signals to the model at the early training steps. For this reason, we decide to warm-up OECL for 50 training epochs with $\mathcal{L}_{\text{contrastive}}$ (i.e., $\alpha = 0$ for the first 50 epochs). The following figure presents training process of class deer in CIFAR-10 with and without warm-up.

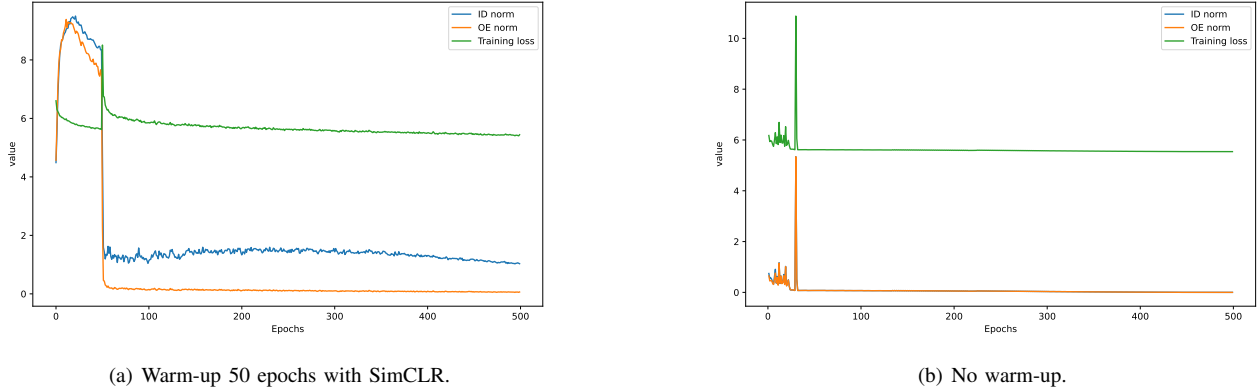


Fig. 8: Training loss and norm of training samples and OE samples during optimization of OECL with and without warm-up.

H. Performance of OECL with different OE datasets the one vs. rest benchmark.

To further illustrate the strengths of OECL, we measure the performance of our proposed method under the unimodal setting with SVHN, DTD and one sample from CIFAR-100 as our non-standard OEs. Table IX shows the overwhelming performance of OECL over HSC for non-standard OE datasets.

TABLE IX: AUC detection performance in % for OECL and HSC on the one vs. rest CIFAR-10 benchmark.

Dataset	OE Dataset	OECL	HSC
CIFAR-10	SVHN	92.2	54.2
	DTD	91.7	82.9
	1-sample CIFAR-100	86.9	50.5

I. Implementation details

We use Resnet [15] along with a 2-layer MLP with batch-normalization and Relu after the first layer. The based contrastive learning module is SimCLR (1) with a temperature of $\tau = 0.5$. We set the balancing hyperparameter $\alpha = 1$ for CIFAR-10 and Imagenet-30 datasets and $\alpha = 0.1$ for DIOR, Raabin-WBC, and HAM10000 datasets. For optimization, we train all models with 500 epochs except self-OECL with 1000 epochs. We adapt LARS optimizer [49] with a weight decay of $1e - 6$ and momentum of 0.9. During the first 50 epochs, we set $\alpha = 0$ as a warming-up phase. For the learning rate scheduling, we use learning rate 0.1 and decay with a cosine decay schedule without restart [30]. We use the batch size of 256 for both normal and OE samples during training, and we detect OOD samples using the ensemble score function s_μ (10) with 32 augmentations. For results on Figure 3 and Figure 7, we use s_{ℓ_2} (9) as our score function. Additionally, we implement global batch normalization [19], which shares batch normalization parameters across GPUs in distributed training setups.

- **CIFAR-10** includes 10 standard object classes with totally 50000 images for training and 10000 images for testing.
- **ImageNet-30** contains 39000 training and 3000 testing images that are divided equally into 30 standard object classes. In leave-one-class-out setting, we randomly selected the following classes: banjo, barn, dumbbell, forklift, nail, parking meter, pillow, schooner, tank, toaster.
- **DIOR** is an aerial images dataset with 19 object categories. Following previous papers [9]; [35], we use the bounding box provided with the data, and select classes that have more than 50 images with dimensions greater than 120×120 pixels. This preprocessing step results in 19 classes, with an average of 649 samples. The class sizes are not equal, with the smallest class (baseballfield) in the training set containing 116 samples and the largest (windmill) containing 1890 samples.

- **Raabin-WBC** is a dataset comprising images of white blood cells categorized into five classes. The training set contains more than 10000 images. For the test set, we choose the Test-A of the dataset [21].
- **HAM10000** is a large collection of dermatoscopic images of common pigmented skin lesions with total 10000 training images. We follow the instruction given by [45], using ISIC2018_Task3_Test_Images.zip (1511 images) for the evaluation purposes.

J. Data augmentations

For data augmentations T and T_{oe} , we use SimCLR augmentations: random crop, horizontal flip, color jitter, and grayscale. We simply set $T_{oe} = T$ in all our experiments. The details for the augmentations are:

- **Random crop.** We randomly crops of the original image with uniform distribution from a to 1.0. We select $a = 0.5$ for Raabin-WBC dataset and Ham10000 dataset, and all the other datasets we set $a = 0.08$. After cropping, cropped image are resized to match the original image size.
- **Horizontal flip.** All training images are randomly horizontally flipped with 50% of probability.
- **Color jitter.** Color jitter changes the brightness, contrast, saturation and hue of images. We implement color jitter using pytorch's color jitter function with brightness = 0.4, contrast = 0.4, saturation = 0.4 and hue = 0.1. The probability to apply color jitter to a training image is set at 80%.
- **Grayscale.** Convert an image to grayscale with 20% of probability.

K. Implementation Details for Other Evaluated Methods

1) *HSC, BCE, Focal, CLIP and BCE-CLIP*: We use the official implementations from [29]. We follow the official setup in their paper in all datasets except for Table IX and Table IV. For the experiment of HSC with 1-sample CIFAR100 as OE, we train it for 200 epochs with milestones at 100 and 150 epochs instead of 30 epochs. So it have same training ground with experiments using SVHN and DTD as OE datasets. For BCE-CLIP configurations on Table IV, we train it for 40 epochs with learning rate reduced by a factor of 10 at milestone 35.

2) *GT and GT+*: We use the official implementations from [18]. For GT+, we encourage the network to have uniform soft-max responses on OE samples.